Supporting Information

Experimental Procedures

Materials

CTAC and Brij-35 were purchased from Sigma Aldrich. Potassium tetrachlorocuprate was purchased from Wako. L-FDLA, L-His and D-His were purchased from TCI. L-Ser and D-Ser were purchased from Shanghai Macklin Biochemical Co., Ltd. Perchloric acid was purchased from General Agent Co., Ltd. Hydrochloric acid was purchased from Sinopharm Chemical Reagent Co., Ltd. Perchloric acid, sodium hydroxide, ninhydrin, deuterium oxide, ethanol, acetone, acetonitrile, potassium chloride, potassium sulfate, nickel chloride lithium citrate, lithium chloride, citric acid, thiodiglycol, benzyl alcohol, propylene glycol monomethyl ether and caprylic acid were purchased from Adamas Reagent. Ammonium bicarbonate was purchased from Alfa Aesar.

Characterization

XRD patterns were recorded on a Rigaku MiniFlex 600 powder diffractometer equipped with Cu Kα radiation (40 kV, 20 mA), at a rate of 0.2° min^{-1} over the range of 20–100°. SEM images were obtained using a Hitachi Regulus 8240 with an accelerating voltage of 5 kV. TEM images were recorded on a JEOL JEM-F200 microscope equipped with a thermal field emission electron gun operating at 200 kV (Cs1.0 mm, Cc 1.1 mm, point resolution of 1.9 Å for TEM, 1.6 Å for STEM) and UHR polepiece. TEM images were acquired using a GATAN OneView IS camera (4,096 × 4,096 pixels). For TEM experiments, almost 100 nm slices of CCFs were cast under ambient conditions onto carbon-coated molybdenum TEM grid**s.** Aberration corrected scanning transmission electron microscopy (AC-STEM) was performed using a probe-corrected Hitachi HF5000 S/TEM, operating at 200 kV. The instrument was equipped with bright field (BF), high angle annular dark field (HAADF) and secondary electron (SE) detectors for high spatial resolution STEM imaging experiments.

The CD spectra were obtained on a JASCO J-1500 spectropolarimeter fitted with a DRCD apparatus, and data were collected with a scanning rate of 20 nm/min ranging from 190 to 800 nm at 293 K. XPS spectra were recorded on a Kratos AXIS UltraDLD spectrometer with a monochromated Al Kα source (1486.6 eV), a hybrid magnification mode analszer and a multichannel detector at a take-off angle of 90° from the plane of the sample surface. The analysis chamber pressure was $<5 \times 10^{-9}$ Torr. All energies are reported as binding energies in eV and referenced to the C 1s signal (corrected to 284.8 eV) for aliphatic carbon on the analysed sample surface. Survey scans were carried out with a 250 ms dwell time and analyser pass energy of 160 eV. High-resolution scans were conducted with a 0.1 eV step size, a dwell time of 100 ms and an analyser pass energy of 40 eV. After background subtraction using the Shirley routine, the XPS spectra were fitted with a convolution of Lorentzian and Gaussian profiles by using Casa XPS software.

Computational details

Density functional theory calculations were performed using the plane-wavebased Vienna Ab Initio Simulation package (VASP)[1]. The wavefunction was expanded in a plane-wave basis set with energy cutoff of 480 eV. The electron exchange and correlation effects were described by the generalized gradient approximation (GGA) in the form of the Perdew–Burke–Ernzerhof (PBE) functional[2]. The D3 correction method was employed to illustrate the long-range dispersion interactions between the adsorbates, water and Cu surface[3]. The interaction between atomic cores and electrons was described by the projector augmented wave (PAW) method[2]. A cut-off energy of 480 eV for the plane-wave basis set and an atomic force convergence of 0.02 eV/Å were employed. A Fermi smearing width of 0.02 eV and dipole corrections were employed as well. For the calculation of all thermodynamic quantities, the open-source atomic simulation environment (ASE)[4] code was used. The Gibbs free energies were calculated at 298 K and 1 atm as outlined below:

$$G = H - TS = E_{DFT} + E_{ZPE} + C_p - TS$$

where E_{DFT} is the DFT-calculated electronic energy, E_{ZPE} is the zero-point vibrational energy, Cp is the heat capacity, T is the temperature, and S is the entropy. Gas-phase molecules such as CO_2 and H_2 were treated using the ideal gas approximation, while adsorbates were treated using a harmonic approximation. The computational hydrogen electrode (CHE) model[5] was used to calculate the Gibbs free formation energy for Ser, ethanol and formic acid intermediates. For example, the Gibbs free energy of formation for OH_2CCO* was calculated as $G_f = G_{OH2CCO*} - (G_{CO + CO*})$. The adsorption energy of each amino acid was calculated as $E_{ads} = E_{AA*} - (E_{slab} + E_{AA})$. The binding energy of CO was calculated as $E_{bind}(CO) = E_{CO*} - (E_{slab} + E_{CO})$. In addition, Gibbs free energies are corrected by experimental conditions (pressure = 4.5MPa, pH = 4.64) according to the previous report[5].

The activation barriers in the stereo-determining step of carbon dioxide reaction were found by the nudge elastic band method with image climbing (CI-NEB)[6], combined with the dimer method[7] to isolate transition states. The NEB method was used to follow the path between the reactant and product states to the point where the perpendicular forces on all of the images along the band were lower than 0.5 eV/Å. The dimer method was subsequently used to isolate the transition state to the point where the force acting on the transition state dimer was lower than 0.05 eV/ Å.

The whole reaction from CO_2 to serine was proposed as follows:

$$3CO_2 + 10H^+ + NH_3 \rightarrow 2CO* + CO_2 + 6H^+ + 2H_2O + NH_3$$

$$2CO* + CO_2 + 6H^+ + 2H_2O + NH_3 \rightarrow H_2CO{\cdot}CO* + CO_2 + 4H^+ + 2H_2O + NH_3$$

$$H_2CO{\cdot}CO* + CO_2 + 4H^+ + 2H_2O + NH_3 \rightarrow H_2CO{\cdot}COCO* + 2H^+ + 3H_2O + NH_3$$

$$H_2CO{\cdot}COCO* + 2H^+ + 3H_2O + NH_3 \rightarrow HOH_2CCOCOOH* + 2H^+ + 2H_2O + NH_3$$

$$HOH_2CCOCOOH* + 2H^+ + 2H_2O + NH_3 \rightarrow HOH_2CCNHCOOH* + 2H^+ + 3H_2O$$

$$HOH_2CCNHCOOH* + 2H^+ + 3H_2O \rightarrow HOH_2CHCNH_2COOH* + 3H_2O$$

The (111) was modelled using (3×3) supercells with a (2×2×1) k-point grid ((1×1×1) k-point grid for small-molecule adsorptions). In addition, the model of the (111) has a 6-atom layer in the z-axis direction and a 15 Å vacuum slab between mirror images in the z-axis in the unit cell.

The (651), (653), (643) and (821) were modelled using (1×2) supercells with a (2×2×1) k-point grid ((1×1×1) k-point grid for small-molecule adsorptions). In addition, the model of the (651), (653), (643) and (821) have 6-atom layer in the z-axis direction and a 15 Å vacuum slab between mirror images in the z-axis in the unit cell.

The (17,5,1) and (13,9,1) were modelled as (1×1) cells with a (2×2×1) k-point grid ((1×1×1) k-point grid for small-molecule adsorptions). In addition, the model of the (17,5,1) and (13,9,1) have with 6-atom layer in the z-axis direction and a 15 Å vacuum slab between mirror images in the z-axis in the unit cell.

The (3,1,17) was modelled using (1×1) supercells with a (2×2×1) k-point grid ((1×1×1) k-point grid for small-molecule adsorptions). In addition, the model of the (3,1,17) has 6-atom layer in the z-axis direction and 15 Å vacuum slab between mirror images in the z-axis in the unit cell.

The (5-31) (one of the $(531)^S$) was modelled using (2×2) supercells with a (2×2×1) k-point grid ((1×1×1) k-point grid for small-molecule adsorptions). In addition, the model of the (5-31) is with 6-atom layer in the z-axis direction and a 15 Å vacuum slab between mirror images in the z-axis in the unit cell.

Analysis of amino acids from CO_2 reduction by amino acid analyser

Amino acids in the products were further analysed by a high-speed amino acid analyser. Before amino acid analysis, 10 mg of purified product was dissolved in 500 μL of 20 mM hydrochloric acid by ultrasonic cleaning for 35 min at 45 ºC. The extract was centrifuged at 15000 rpm for 15 min, filtered through a 0.22 μm membrane, and stored for amino acid analysis. The analysis of amino acids was carried out by using an L-8900 amino acid analyser (Hitachi, Japan). An ion-exchange chromatographic column (L-8900, Hitachi, Japan) was adopted, where the amino acids were eluted by a lithium buffer system of an amino acid analyser (Tables S1and S2). After reacting with 500 μL of ninhydrin solution (979 ml of propylene glycol monomethyl ether, 39 g of ninhydrin, 81mg of sodium hydroxide), the resultant derivatives were measured by UV detection at two wavelengths of 440 and 570 nm simultaneously. Due to a low response at 570 nm, the derivative of proline was detected at 440 nm. Quantification of amino acids was performed using mixed amino acid standard solutions of Type B and Type AN-2 (Wako) using the same method mentioned above.

Composition of buffer solution for amino acid analysis.*

Name	PF-1	PF-2	PF-3	PF-4	PF-RG
Vessel (buffer)	B1	B2	B3	B4	B5
Lithium Concentration (N)	0.09	0.255	0.721	1	0.2
Distilled water (ml)	700.0	700.0	700.0	700.0	700.0
Lithium citrate ($4H_2O$) (g)	5.73	9.80	8.79	9.80	0
Lithium chloride (g)	1.24	6.36	26.62	38.15	0
Citric acid (H_2O) (g)	19.90	12.00	11.27	3.30	0
Ethanol (ml)	30.0	30.0	100.0	0	30.0
Thiodiglycol (ml)	5.0	5.0	0	0	0
Benzyl alcohol (ml)	0	0	3.0	0	0
Brij-35* (ml)	4.0	4.0	4.0	4.0	4.0
pH (nominal)	2.8	3.7	3.6	4.1	/
Total (adjust) (L)	1.0	1.0	1.0	1.0	1.0
Caprylic acid (ml)	0.1	0.1	0.1	0.1	0.1

Time (min)	%B1	%B2	%B3	%B4	%B5	Column Temp.
0	100	0	0	0	0	38
2.0	100	0	0	0	0	30
21.5	100	0	0	0	0	
21.6	100	0	0	0	0	60
33.5	70	30	0	0	0	
33.6	10	90	0	0	0	
36.5	10	90	0	0	0	40
43.5	0	100	0	0	0	
43.6	0	100	0	0	0	
50.5	0	100	0	0	0	70
50.6	0	0	100	0	0	
68.4	0	0	100	0	0	45
69.5	0	0	100	0	0	
69.6	60	0	0	40	0	
75.0	60	0	0	40	0	
75.1	0	0	0	100	0	
82.0	0	0	0	100	0	
82.1	0	20	0	80	0	
92.5	0	20	0	80	0	70
99.5	0	20	0	80	0	
99.6	0	0	0	100	0	
112.5	0	0	0	100	0	38
112.6	0	0	0	0	100	
140.0	0	0	0	0	100	38

Time-dependent mobile phase conditions and column temperatures for amino acid analysis.

***Dissolve 25 g of amino acid into 100 ml of distilled water.**

Detail of PIMS equipment and analysis conditions

Beamline

The experimental investigations were carried out at the combustion beamline (BL03U) of the National Synchrotron Radiation Laboratory (NSRL) in Hefei, China. Synchrotron radiation from the undulator beamline was monochromatized with a 200 lines/mm laminar grating (Horiba Jobin Yvon, France), which covered the photon energy from 7.5 to 22 eV with an energy resolving power of 3000 (E/ΔE @ 10 eV). The average photon flux could reach a magnitude of 10^{13} photons/s after suppressing the higher order harmonic radiation by a gas filter filled with noble gas[8].

Apparatus for in situ analysis of CO_2 electroreduction products and schematic diagram of the PIMS equipment connected to the reactor.

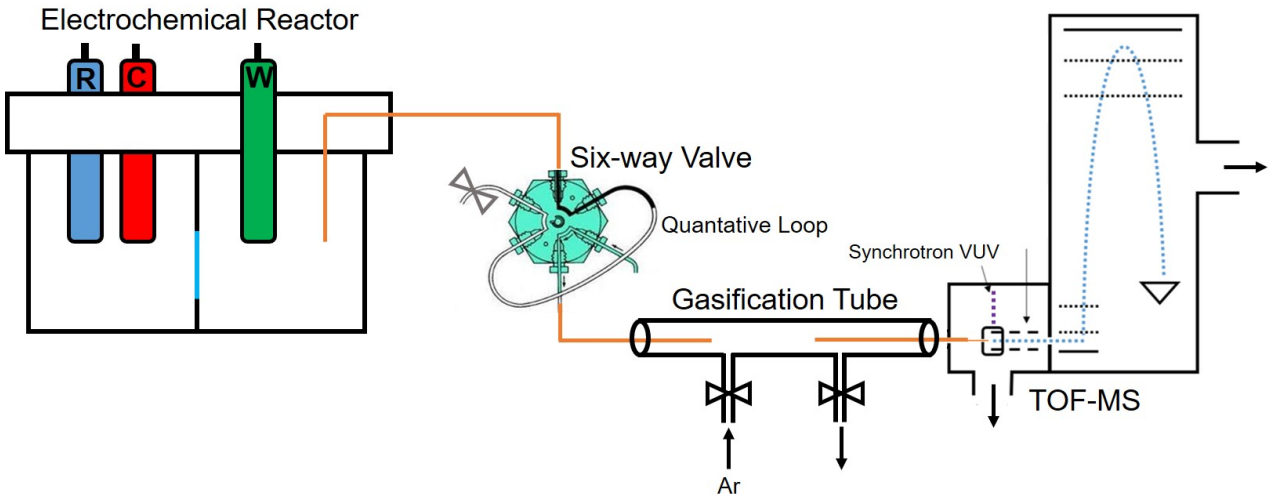

The apparatus for in-situ analysis of CO_2 electroreduction products consists of a high-pressure electrochemical reactor, a six-way valve, a gasification tube and a home-made reflection time-of-flight mass spectrometer (RTOF-MS)[9-11]. The reaction was monitored online for 24 h and analysed every hour. For each test, the sample solution was pushed into the 250 μl sample loop of the six-way valve for 5 min by the high pressure of the reactor every hour, and argon (99.999%) was used to push this solution into a gasification tube after the six-way valve was switched. Then the sample solution was vapourized in a gasification tube that was heated at 280 °C. The gaseous products were introduced into the ionization zone of the RTOF-MS and ionized by the vacuum ultraviolet (VUV) light. Ions were focused into the mass analyzer and detected by a micro-channel plate detector. DHO was selected as inner standard compound because it would not interference the CO_2 reduction and be stable in whole experiments.

Quantitative tests of products were performed by in situ PIMS at the National Synchrotron Radiation Laboratory (NSRL) in Hefei, China. Because of high concentration of NH_4HCO_3, PIMS was employed in this work to prevent corrosion and contamination from NH_3 and CO_2 at high temperatures. Both gaseous and liquid products were extracted from the electrochemical reactor and analysed by in situ PIMS every hour. The experimental setup is described in Fig. S1. The photon energy was set at 12.5 eV, and 99% argon was employed as the carrier gas. Each product was quantified by using DHO (m/z = 19.02) as an internal standard compound. According to previous literature[12-15], the species mole fraction (X_i) of each product from CO_2 reduction was calculated.

$$X_i = X_{DHO}[S_i/S_{DHO}][\sigma_{DHO}/\sigma_i][D_{DHO}/D_i]$$[12]

X_i is the species mole fraction; S_i is the ion signal (integrated ion counts); σ_i is the photoionization cross-section at the photon energy E = 12.5 eV; and D_i is the mass discrimination factor for each species (more details were represented in supplementary information). The σ_i of ethanol[12], formic acid[13], 3-hydropyruvic acid, Ser[14] and DHO[15] were validated from previous reports.

Schematic illustration of the strategy for enantioselective synthesis of amino acids on chiral Cu surfaces

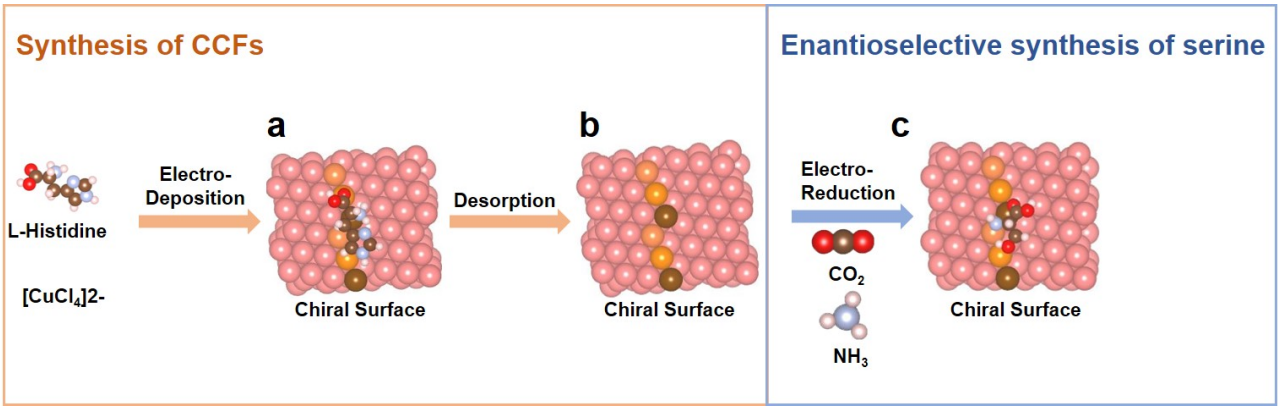

Fig. S1 | Strategy for the synthesis of CCFs and enantioselective synthesis of amino acids. **a,** Electrodeposition of CCFs with chiral kink sites induced by His. **b,** Elimination of His on surfaces through CV. **c,** CO_2 electroreduction with NH_3 participates in the reaction.

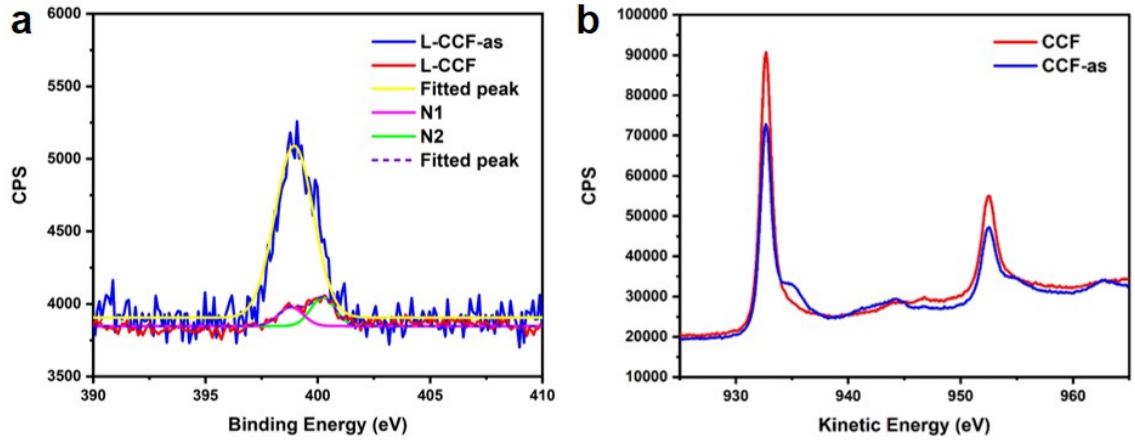

Fig. S2 | Comparison of N 1s XPS of L-CCFs-as and L-CCFs.

As shown in Figure S2a, the XPS peak position (399.0 eV) of L-CCFs-as is corresponding to His adsorbed on Cu surfaces (Fig. S13a). In XPS of L-CCFs, nitrogen peak N 1s (399.0 eV corresponding to His) was weaken and another weak peak appeared in 400.1 eV, which indicates His was almost removed by electrochemical treatment and thiourea or cyanide were formed[16,17]. Two peaks at 398.8 eV (N1) and 400.1 eV (N2) can be evaluated for fitting XPS of L-CCFs, which can be attributed to trace residue L-His and ammonium salt or cyanide decomposed from His, respectively (Fig. S13a). We calculated stoichiometric ratios from the peak areas of Cu $2p_{2/3}$ and N 1s of L-CCFs-as and L-CCFs. It was revealed that N/Cu of L-CCFs-as is 0.0439, while N/Cu of L-CCFs is 0.0018 (N1) and 0.0028 (N2), indicating parts of L-His were decomposed into cyanide or ammonium salt and residue on L-CCF are almost removed by electrochemical treatment.

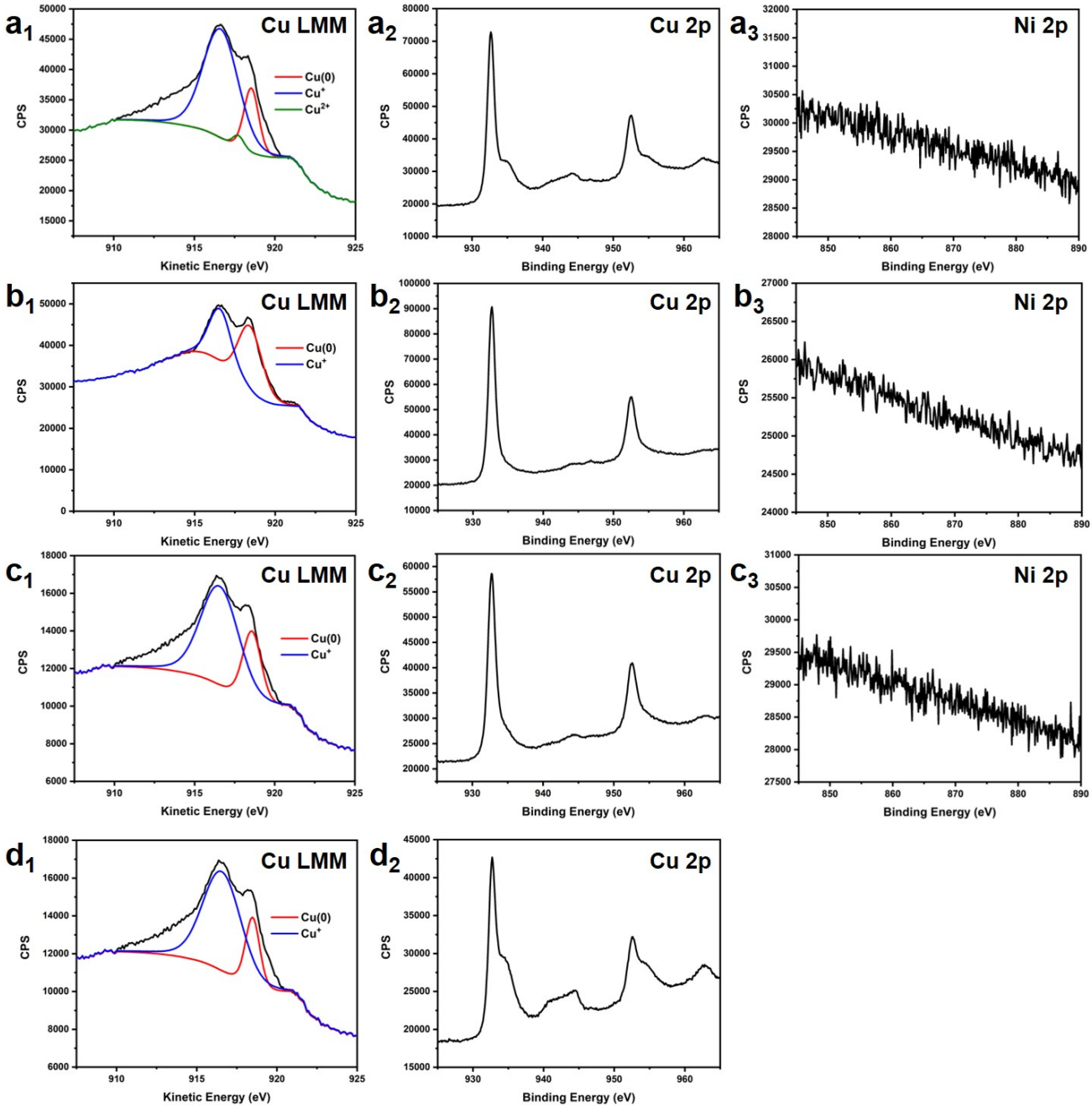

Fig. S3 | Cu LMM XPS of L-CCF-as (a), L-CCF (b) ACF (c) and Cu foil (d).

The chemical composition of CCFs was analysed by comparing the XPS spectra of CCFs-as and the final CCFs after removing the organics. In the Cu LMM Auger spectrum of L-CCFs-as, Cu LMM peaks located at 918.6 eV, 916.8 eV and 917.7 eV corresponding to Cu^0, Cu^{1+} and Cu^{2+} [18], respectively, were observed, while in contrast, only peaks corresponding to Cu(0) and Cu^{1+} could be observed in the Cu LMM XPS spectra of the final L-CCFs. This account for the partly oxidized Cu surfaces during removal and reduction by electrochemical cleaning. Although the Cu^{1+} peak was observed in the Cu LMM spectra of L-CCFs, considering that there were no peaks attributed to Cu_2O in the XRD pattern of L-CCFs, very little Cu^{1+} was present on the surfaces of L-CCFs. In the Cu LMM spectra of ACFs, there were only peaks corresponding to Cu^0 and Cu^{1+}, indicating that the Cu states of the CCF and ACF surfaces were almost the same. In auger spectra of as-made L-CCFs-as (Fig. S3a1), the peaks position of Cu^0 and Cu^{1+} is broader and more continuous than that of other spectra. With only the addition of Cu^{2+} peak the peaks fitted well in Fig. S3a_1, indicating the presence of Cu^{2+} in the Auger spectra of L-CCFs-as. There were no peaks corresponding to Ni 2p located at 852.6 eV, 853.1eV and 858.3 eV[19] detected in either CCFs and ACFs (Fig. S1a_3, Fig. S2 a_3, b_3), indicating that Ni was not codeposited with Cu on the substrate.

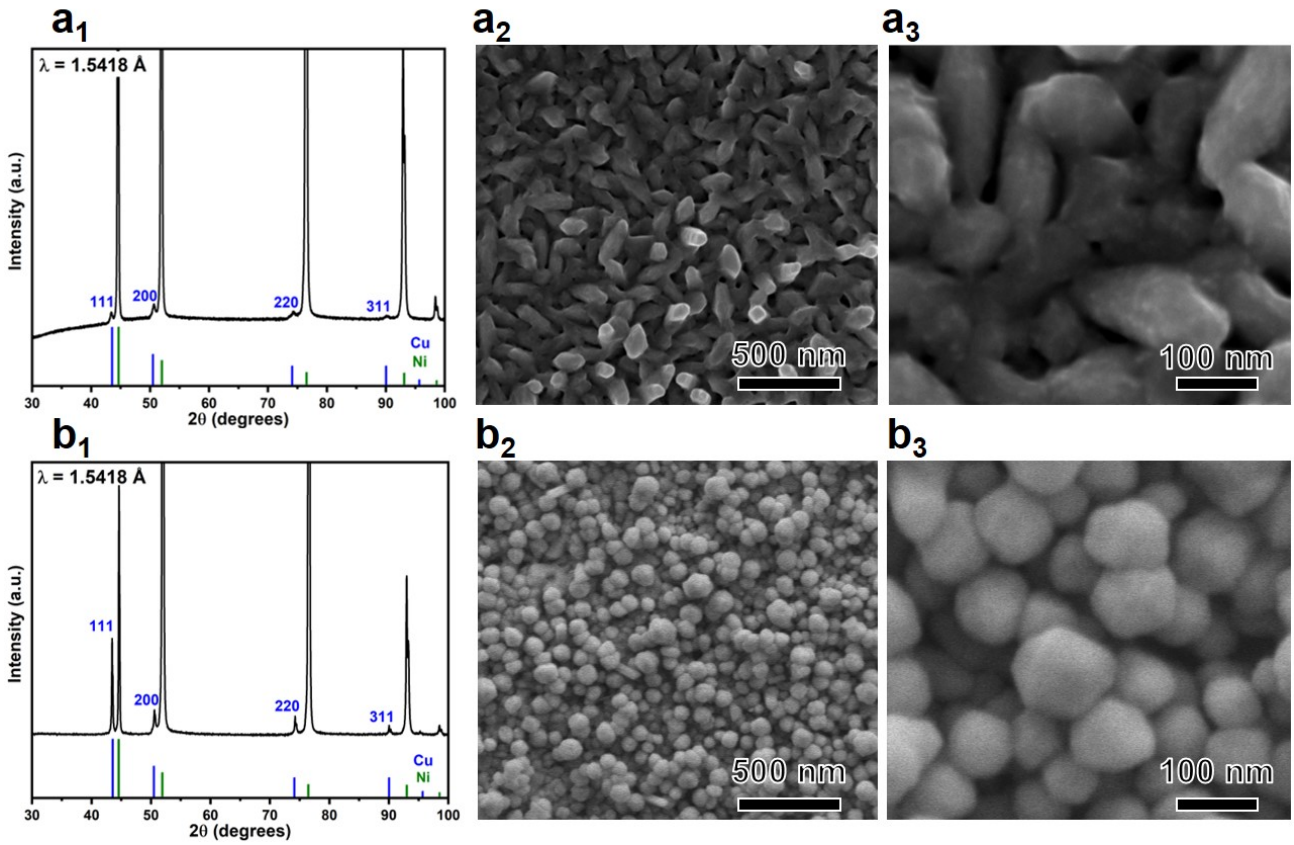

Fig. S4 | XRD patterns and SEM images of D-CCF ($a_{1\text{-}3}$) and ACF ($b_{1\text{-}3}$).

As shown in the XRD patterns and SEM images, the morphology of Cu crystals and their growth orientation of D-CCFs and L-CCFs were almost the same. However, the polyhedral morphology of Cu nanoparticles was different from that of the CCFs observed in ACFs, and the relative intensity of the 111 reflection in the XRD pattern of ACFs was the same as that of the bulk sample, indicating the characteristic crystal growth along the 111 plane with close stacking.

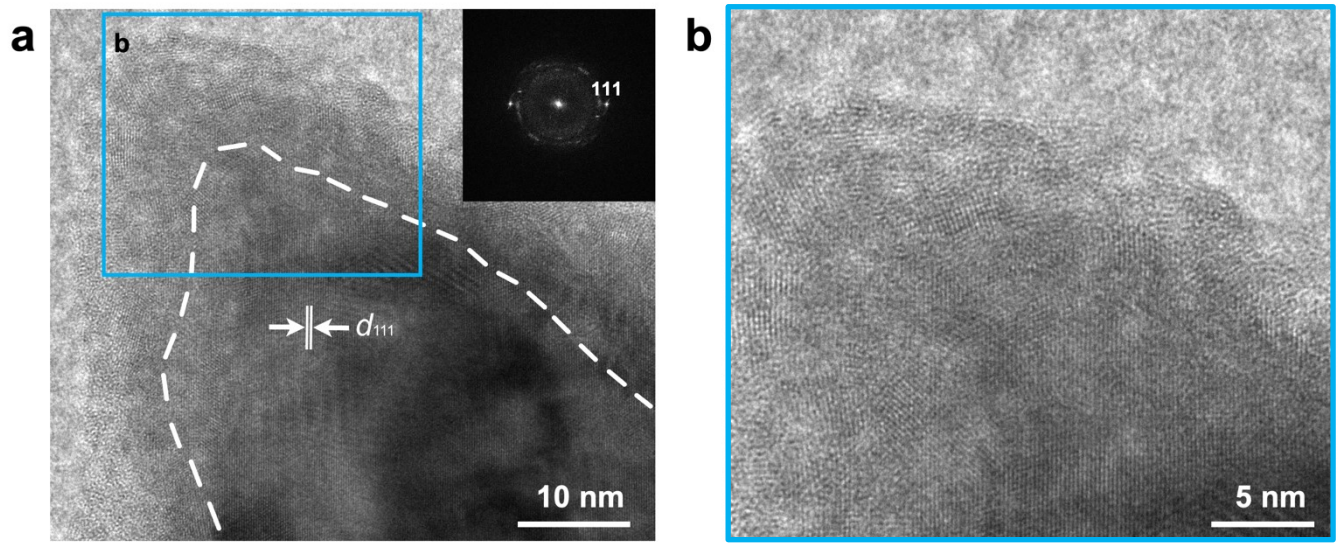

Fig. S5 | The HRTEM image of polycrystalline nanocrystals surrounding a single crystalline core of fusiform Cu nanoparticles in L-CCFs.

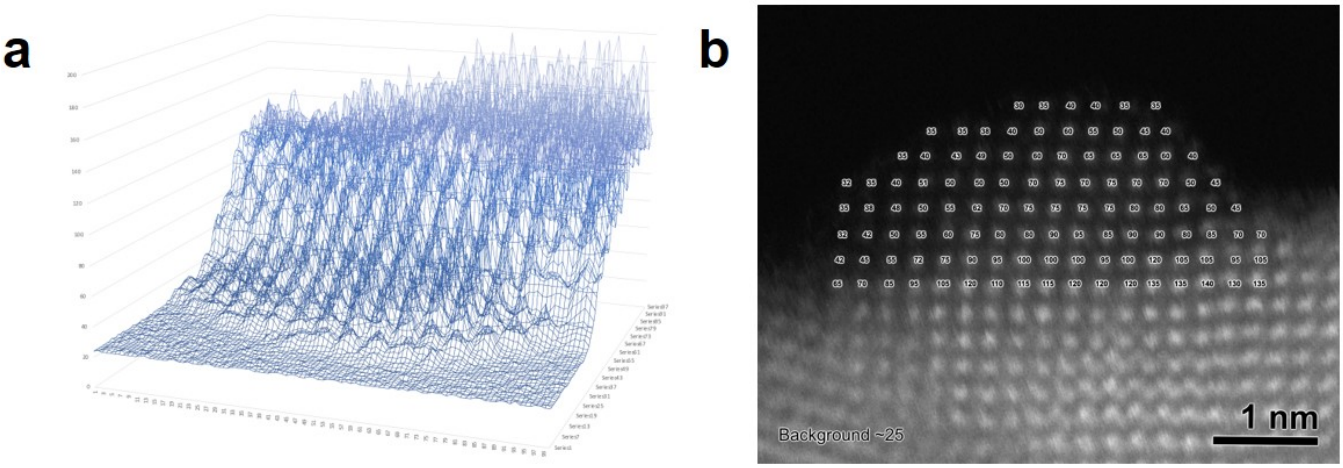

Fig. S6 | Intensity profile of the STEM-HAADF image (a) and the number of atoms determined in the HAADF-STEM image (b) of CCFs, as shown in Fig. 1d.

The intensity of each point in the STEM-HAADF image was extracted by the intensity profile tool in Gatan DigitalMicrograph. The background level is ~25. Each peak suggests a column of atoms. The peak value was used to determine the atom numbers in each column. The value in the profile was divided by a common divisor 5 so that the atomic number for all the columns can be an integer and the smallest number is 1 atom. The number of atoms in each column is shown in Table S1. The numbers overlaid on the column of atoms show the extracted intensity from the original image. As the observed intensity (brightness) of the column of atoms is linearly correlated to the atomic number.

Table S1 | Number of atoms along the z-axis direction in each column of atoms extracted from the HAADF-STEM image.

1st layer	2nd layer	3rd layer	4th layer	5th layer	6th layer	7th layer
3	1	2	1	0	0	0
4	3	3	2	0	0	0
6	5	5	3	2	0	0
9	6	5	5	3	2	0
10	7	6	5	4	2	0
13	10	7	5	5	3	0
14	11	9	5	5	3	1
15	11	10	9	7	5	2
15	13	10	10	9	7	3
15	14	10	9	8	6	3
14	12	10	10	8	5	2
15	13	11	9	8	4	2
19	13	11	9	7	3	0
16	11	8	5	3	0	0
16	12	5	4	0	0	0
14	9	4	0	0	0	0
16	9	0	0	0	0	0

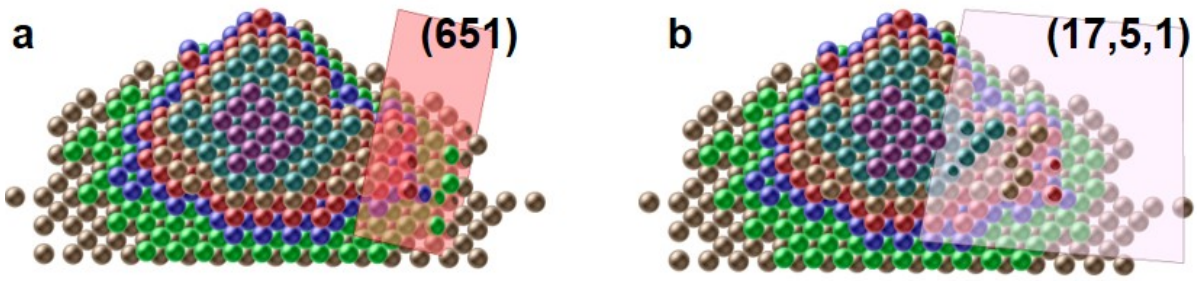

Fig. S7 | Slab surface models of (651) (a) and (17, 5, 1) (b).

It is worthy to note that (651) and (17,5,1) can also be approximatively identified from the model shown in Fig. 1e in main text, however, integrated atomic arrangements could not be observed in their slab surface models. Considering the morphology of the sample without distinct crystal facts, there is possibilities of various chiral surfaces.

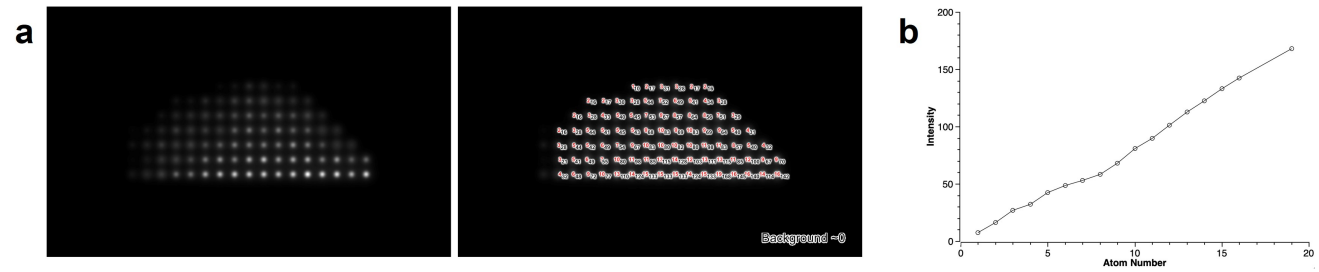

Fig. S8 | Simulated HAADF-STEM image (a) from the structural model along [001] direction. The red numbers are corresponding to the number of Cu atoms in the columns. The white numbers are the intensity extracted from the simulated image. The background is almost 0; (b) The relationship between the intensity and atom number. A value of ~7.5 is calculated for the unit intensity for each Cu atom.

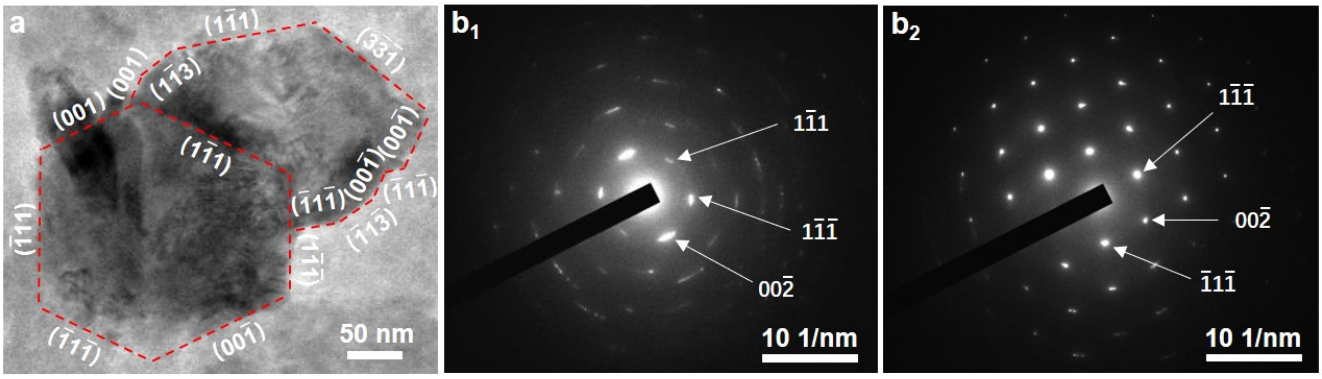

Fig. S9 | TEM image (a) and SAED images (b) of ACFs. b_1 corresponds to the left nanoparticle, and b_2 corresponds to the right nanoparticle, respectively. All the observed crystal faces can be assigned to low Miller index lattice planes.

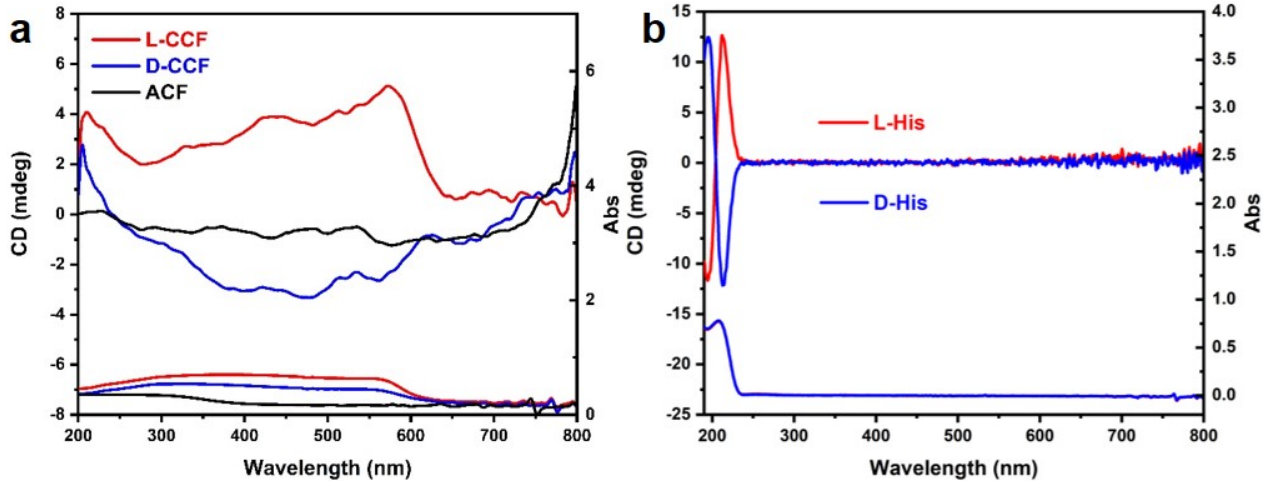

Fig. S10 | CD spectra of antipodal CCFs and ACFs (a) and antipodal His aqueous solution (20 μg/ml) (b).

The DRCD spectra (Fig. S10a) of L- and D-CCFs show positive and negative broad peaks at 300-600 nm, respectively. The TCD spectra (Fig. S10b) of the antipodal His show mirror-image CD signals at 200~250 nm corresponding absorption of His. It can be seen that there are no signals matching with both CD and UV-Vis adsorption signals of L-His or D-His (Fig. S10b) in the spectra of antipodal CCFs (Fig. 10a). This result indicates that no His residue in CCFs after electrochemical treatment. Almost no peaks were observed in the CD spectra of ACFs, which indicates that no symmetry breaking occurred in it.

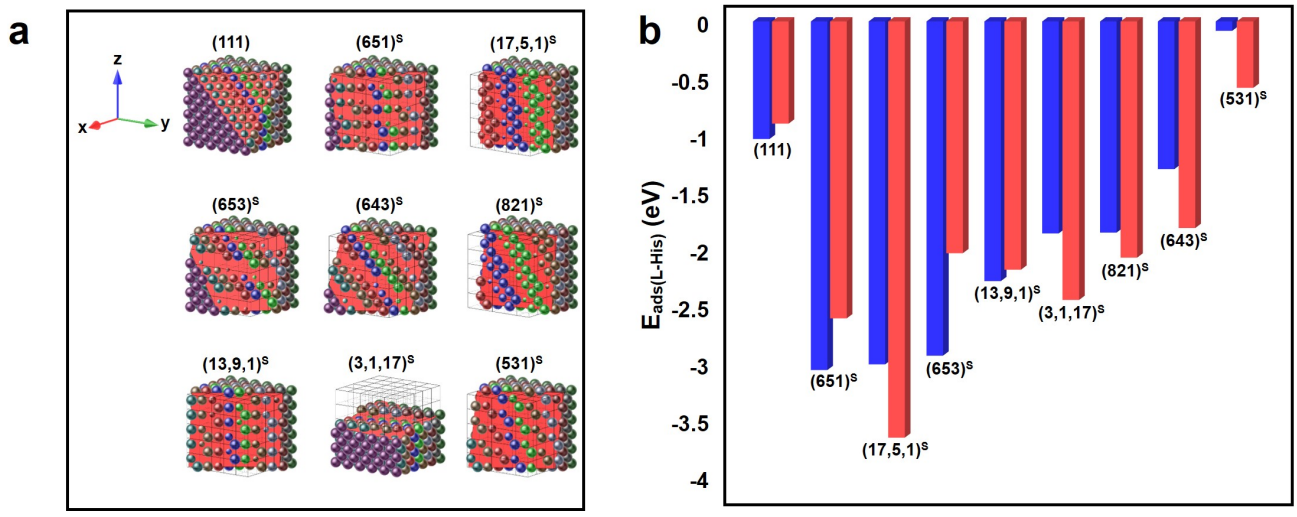

Fig. S11 | Formation possibility of chiral Cu surfaces on CCFs. a, Schematic illustration of the ideal atomic models Cu(111) and the possible chiral kink sites Cu(651)^S, (17,5,1)^S, (653)^S, (643)^S, (821)^S, (13,9,1)^S, (3,1,17)^S and (531)^S. **b,** Adsorption energies predicted by DFT calculations for L-His (blue) and D-His (red) on the Cu surfaces, in which the unit cell contains one adsorbed molecule

Table S2 | Thermodynamic quantities used in DFT calculations for the adsorption energy of L-His on each chiral kink site.

Surface-Molecule	E_{elec} (eV)	E_{ads} (eV)	E_{mol} (eV)	E_{slab} (eV)
(1 1 1)^S-L-His	-999.493	-1.031	-126.176	-872.286
(13 9 1)^S-L-His	-580.81	-2.277	-126.176	-452.357
(17 5 1)^S-L-His	-575.566	-3.007	-126.176	-446.383
(3 1 17)^S-L-His	-1024.115	-1.859	-126.176	-896.08
(5 3 1)^S-L-His	-685.1	-0.082	-126.176	-558.842
(6 4 3)^S-L-His	-1274.94	-1.295	-126.176	-1147.469
(6 5 1)^S-L-His	-754.78	-3.057	-126.176	-625.547
(6 5 3)^S-L-His	-891.286	-2.931	-126.176	-762.179
(8 2 1)^S-L-His	-750.628	-1.852	-126.176	-622.6

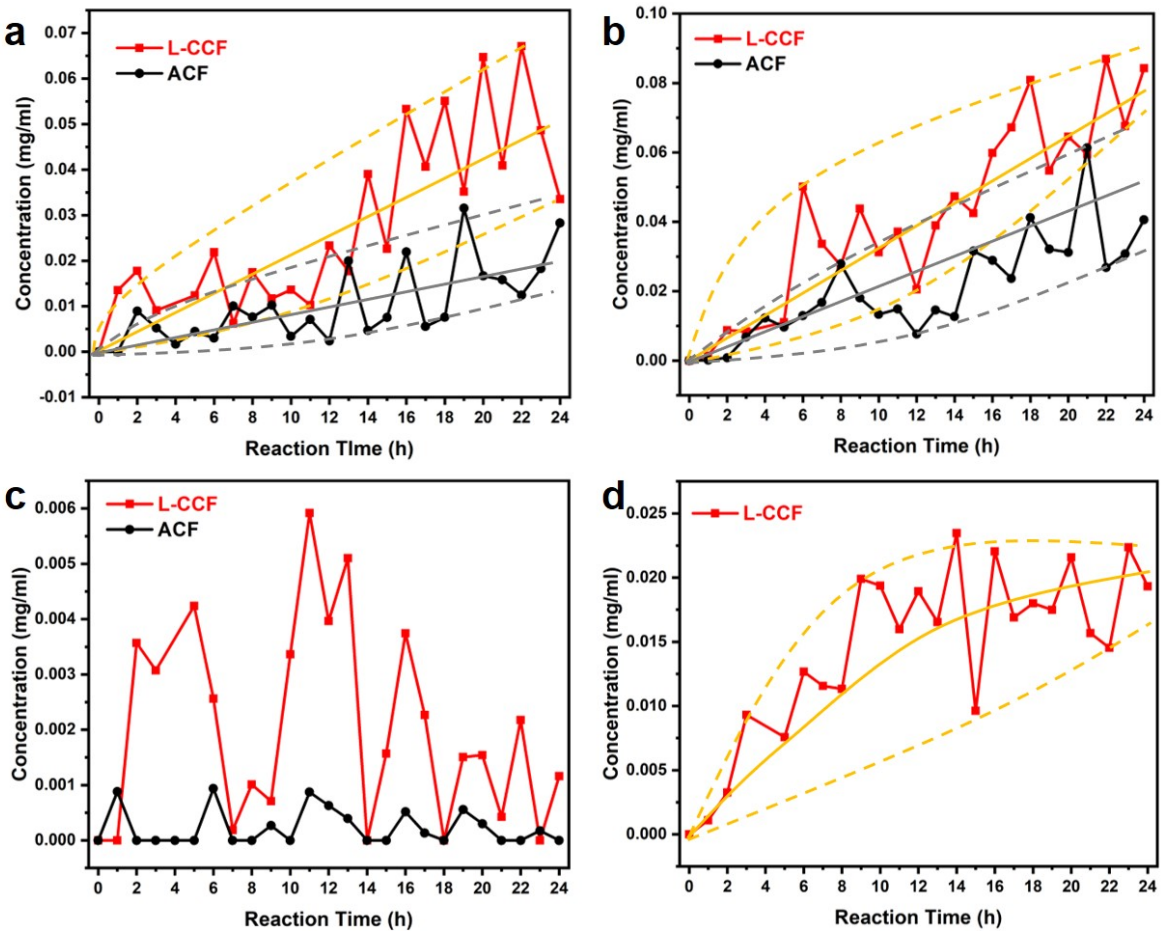

Fig. S12 | Time-dependent concentrations of ethanol (m/z = 46.04, 45.03) (a), formic acid (m/z = 46.01) (b), 3-hydroxypyruvic acid (m/z = 104.01) (c) and serine (m/z = 105.04) (d) observed by PIMS in the electrocatalytic reaction.

The orange solid line and dotted line represent the trend and possible range of product amounts catalyzed on L-CCFs, and the grey solid line and dotted line present the trend and possible range of product amounts catalyzed on ACFs in 0.25 M NH_4HCO_3 under 4.5 MPa CO_2.

Table S3 | Molar number of amino acids in products from different catalysts and various reaction conditions.

Molar Number (nmol)	L-CCF	ACF	ACF-L-His*	L-CCF (x = -0.6 V)#	L-CCF (x = -0.7 V)#	L-CCF (x = -0.8 V)#	L-CCF (x = -0.9 V)#	L-CCF (x = -1.0 V)#	Blank&
P-Ser	11.2	4.9	0.7	1.3	7.1	2.5	4.3	2.6	0.0
Urea	312.2	270.6	110.2	344.5	316.4	268.9	568.8	307.9	0.0
Asp	2.8	6.1	7.8	8.3	27.4	13.8	21.6	27.5	0.7
Thr	0.0	4.9	6.0	7.8	23.7	14.6	17.4	24.2	0.0
Ser	2661.9	29.4	29.0	42.1	94.0	68.5	91.4	120.6	0.8
Glu	0.0	3.3	3.1	3.4	17.6	8.0	9.8	8.4	0.0
Gly	73.0	22.8	21.8	31.08	89.4	52.1	68.4	80.2	0.0
Ala	38.4	13.4	16.9	21.33	69.1	32.4	36.5	55.5	0.0
Val	14.6	4.4	4.5	7.8	20.1	11.1	13.6	17.4	0.0
Cys	0.0	0.0	0.0	0.0	0.0	0.0	0.0	0.0	0.0
Met	0.0	0.0	0.0	0.0	0.0	0.0	0.0	0.0	0.0
Ile	8.0	2.9	2.5	10.5	10.8	6.7	8.4	14.3	0.0
Leu	7.8	3.3	2.8	7.1	16.4	6.7	10.6	14.2	0.0
Tyr	2.2	1.9	1.4	0.6	5.2	3.6	6.2	6.6	0.0
Phe	2.4	1.2	0.0	0.2	5.0	3.5	4.9	4.6	0.0
g-ABA	4.4	0.0	0.5	0.3	3.7	0.0	0.6	0.7	0.0
Orn	12.4	9.8	11.1	15.6	28.6	19.3	34.7	45.7	0.0
Lys	5.8	2.9	2.4	3.3	9.1	5.1	9.3	11.7	0.0
His	2.8	3.8	126.5	5.6	10.8	7.8	8.8	16.6	0.0
Arg	0.0	0.0	0.0	0.0	4.2	0.0	2.1	0.0	0.0
Pro	0.0	0.0	0.0	0.0	0.0	0.0	0.0	11.7	0.0

* Sample ACF-L-His：ACFs with L-His adsorbed on the surfaces (1 ml of 1 mg/ml L-His aqueous solution dropped on a10*15 mm ACFs, then dried at room temperature for 12 hours, and then rinsed in ethanol.

Catalysis by applying a constant potential instead of CV, where x is the applied potential.

& Blank is the control experiment that uses 0.25 M NH_4HCO_3 as reaction solution under 4.5 MPa CO_2 at room temperature for 24 h.

Table S3 shows that a significant number of Ser and various amino acids with nanomolar scales could be formed using L-CCFs as electrocatalysts. Nanomole-scale urea and other amino acids could be synthesized using ACFs as electrocatalysts. Notably, the amount of Ser formed on the L-CCFs was 100 times that formed on ACFs, indicating that CCFs could selectively and efficiently catalyze amino acids much more than ACFs.

By applying a constant potential, only nanomole-scale amino acids could be synthesized using L-CCFs as the catalyst. CO_2 is speculated to be synthesized on both chiral kink steps and 111 plane surfaces on L-CCFs. In strong contrast, when applying a changing potential, local chemical conditions on the electrode surface will change transiently[20]. Adsorbents could diffuse onto chiral kink sites and be reduced into amino acids at a lower cathodic potential, and then amino acids could be desorbed from chiral kink sites at a higher cathodic potential. This means that the interference of the 111 plane surfaces could be effectively suppressed and result in the higher yield and *ee* value of Ser from CO_2 electroreduction. The possibility of contamination from the environment and spontaneous CO_2 reduction under 4.5 MPa CO_2 in all CO_2 electroreduction experiments in this work was excluded in the control experiment.

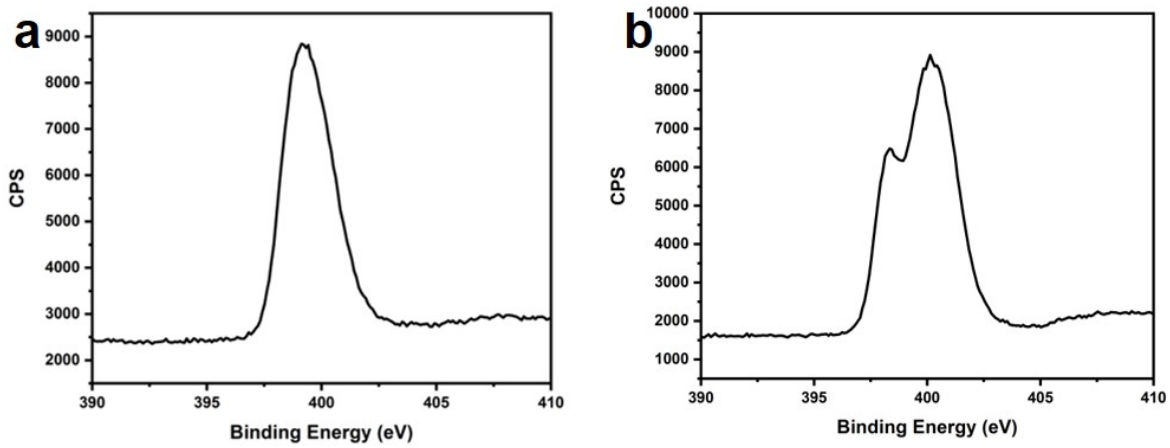

Fig. S13 | N 1s XPSs of ACF-L-His (a) and powder L-His (b).

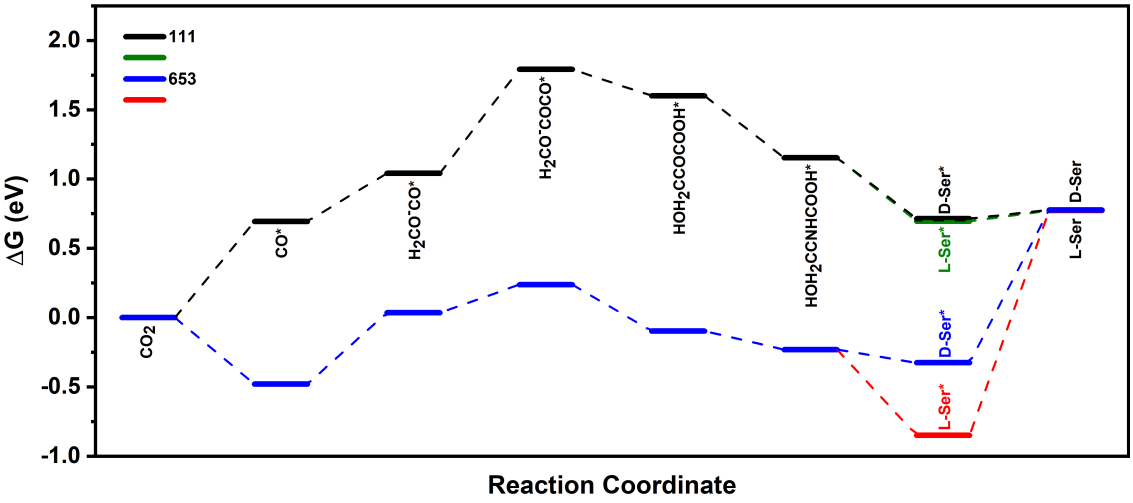

Fig. S14 | Gibbs free energy profile corrected by the pressure of 1 atm (≈0.101325 MPa)

Fig. S14 shows the Gibbs free energy profiles for the intermediates of CO_2 reduction on $Cu(653)^S$ and Cu(111) at 1 atm. In this Gibbs free energy profiles, the Gibbs free energy of $H_2CO^*COCO^*$ formation from $H_2CO^*CO^*$ on $Cu(653)^S$ is 0.203 eV, which is lower than 0.546 eV of Cu(111). This result indicates that the serine formation is also thermodynamic preferable on $Cu(653)^S$ than Cu(111) at standard atmospheric pressure.

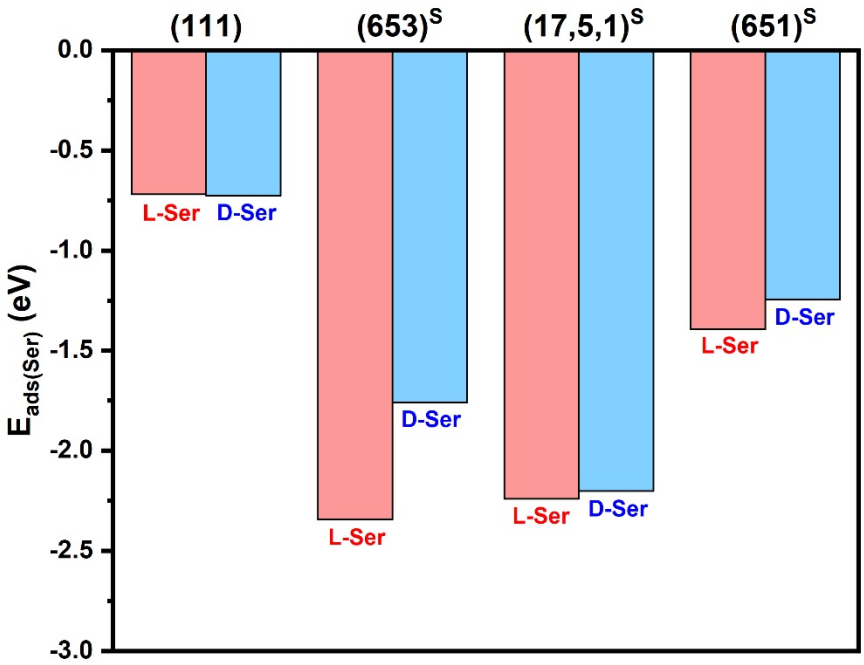

Fig. S15 | Adsorption energies predicted by DFT calculations for L-Ser and L-Ser on various chiral Cu kink sites, in which the unit cell contains one adsorbed molecule.

Table S4 | Gibbs free energies of serine and intermediate formation from CO_2 and NH_3.

Crystal faces	Cu(653)^S	Cu(111)
E_{bind} (CO) (eV)	-1.752	-0.742
ΔG_{f1} (eV)	0.515	0.348
ΔG_{f2} (eV)	0.203	0.749
ΔG_{f3} (eV)	0.270	-0.190
ΔG_{f4} (eV)	-0.739	-0.448
ΔG_{f5} (eV)	-0.619 (L), -0.095 (D)	-0.457 (L), -0.439 (D)

Table S5 | Thermodynamic quantities used in DFT calculations for serine formation from CO_2 and NH_3.

Adsorbates on Cu(653)^S	G (eV)	ZPE (eV)	TS (eV)	Cp (eV)
L-Ser*	-81.380	3.039	0.486	0.240
D-Ser*	-80.856	2.971	0.474	0.225
CO* + CO*	-32.280	0.352	0.167	0.094
CO*	-16.387	0.175	0.060	0.036
H_2CO-CO*	-37.532	1.025	0.177	0.085
H_2CO-COCO* + H2O	-68.490	1.848	0.445	0.232
$HOOCCOCH_2OH$*	-68.825	1.954	0.328	0.203
$HOOCCNHCH_2OH$*	-73.935	2.340	0.425	0.216

Adsorbates on Cu(111)	G (eV)	ZPE (eV)	TS (eV)	Cp (eV)
L-Ser*	-79.834	2.986	0.514	0.243
D-Ser*	-79.816	2.985	0.468	0.223
CO* + CO*	-31.106	0.358	0.312	0.156
CO*	-15.422	0.173	0.147	0.078
H_2CO-CO*	-36.590	1.023	0.243	0.108
H_2CO-COCO* + H2O	-66.876	1.551	0.231	0.130
$HOOCCOCH_2OH$*	-67.109	1.987	0.433	0.206
$HOOCCNHCH_2OH$*	-72.551	2.377	0.586	0.290

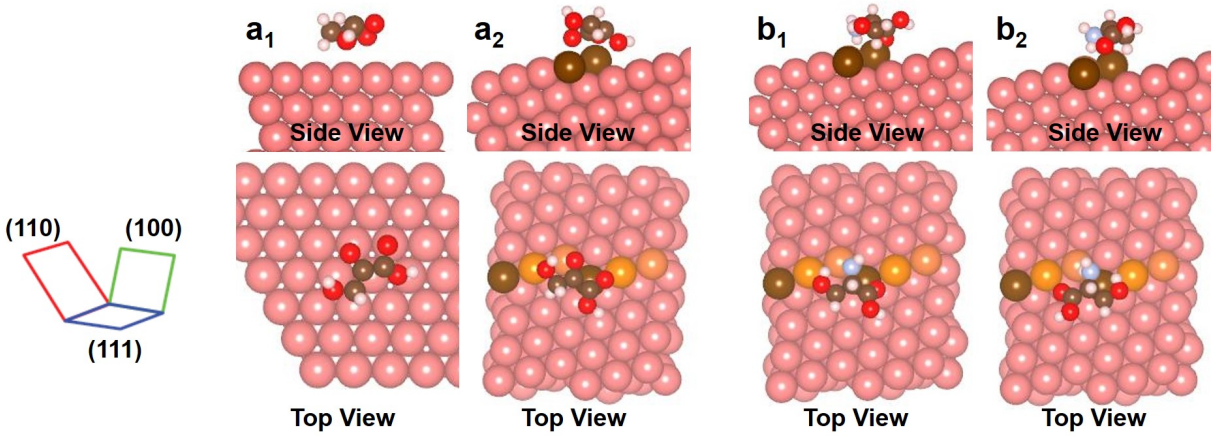

Fig. S16 | Atomic models of 3-hydropyruvic acid adsorbed on Cu(111) (a_1) and Cu(653)^S (a_2); L-Ser (b_1) and D-Ser (b_2) adsorbed on Cu(653)^S.

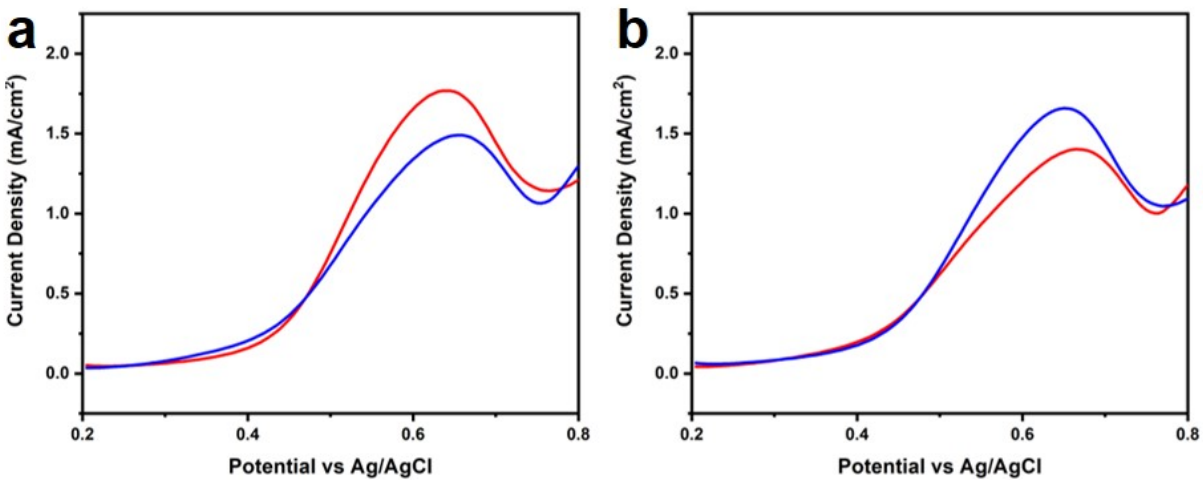

Fig. S17 | DPV of the electrooxidation of 5 mM L-Ser (red) and D-Ser (blue) in 0.1 M NaOH as a supporting electrolyte with different electrodes: (a) L-CCFs and (b) D-CCFs.

To further investigate the enantioselective properties of CCFs, differential pulse voltammetry (DPV) was employed for the enantioselective oxidation of L- and D-Ser. The signal of amidogen oxidation in serine was observed between 0.6 and 0.8V[21]. While L-CCFs shows a higher amplitude for L-Ser than for D-Ser, D-CCFs shows a higher amplitude for D-Ser than for L-Ser. These results confirm that CCFs could be prepared using a chiral template and exhibit enantioselectivity for each enantiomer of Ser.

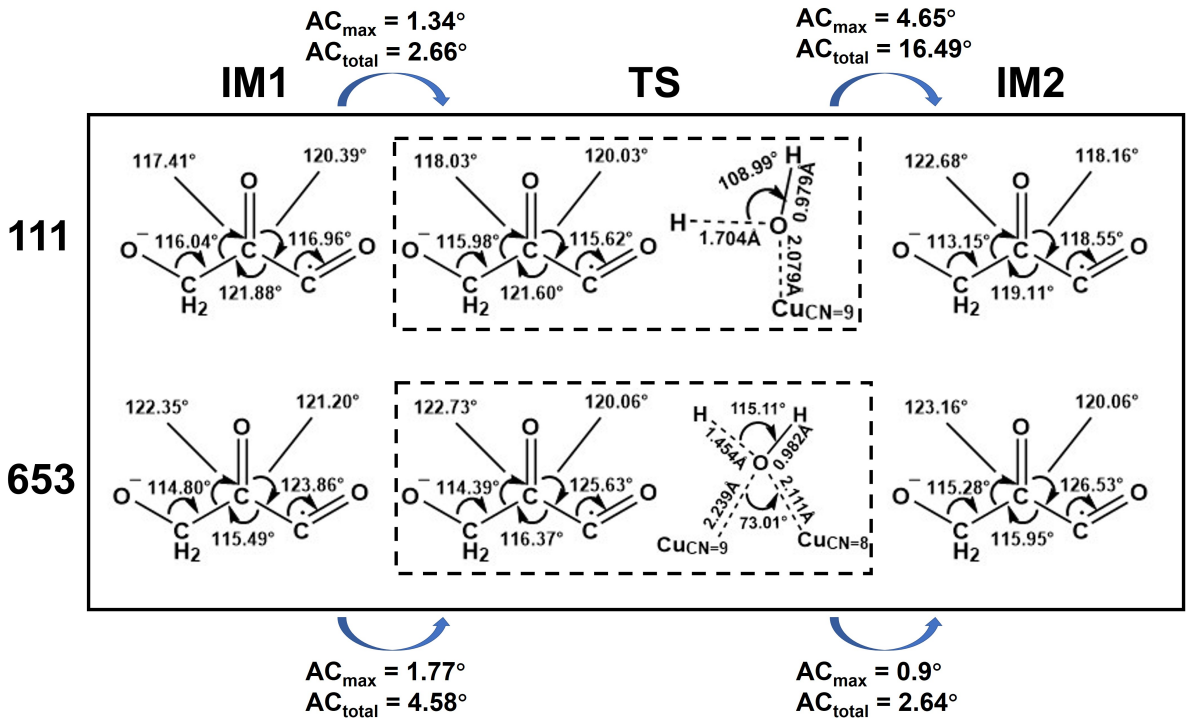

Fig. S18 | Description of amounts of bond angle change in the process of synthesis from IM1 to IM2, AC_{max} represents the highest amount of bond angle change between two molecular models, AC_{total} represents the total amount of bond angle change between two molecular models.

References

1 Perdew, J. P., Burke, K. & Ernzerhof, M. Generalized gradient approximation made simple. *Phys. Rev. Lett.* **77**, 3865-3868 (1996).

2 Kresse, G. & Joubert, D. From ultrasoft pseudopotentials to the projector augmented-wave method. *Phys. Rev. B*. **59**, 1758-1775 (1999).

3 Grimme, S. et al. A consistent and accurate ab initio parametrization of density functional dispersion correction (DFT-D) for the 94 elements H-Pu. *J. Chem. Phys.* **132**, 154104 (2010).

4 Hjorth, L. A. et al. The atomic simulation environment—a Python library for working with atoms. *J. Phys. Condens. Matter.* **29**, 273002 (2017).

5 Nørskov, J. K. et al. Origin of the overpotential for oxygen reduction at a fuel-cell cathode. *J. Phys. Chem. B.* **108**, 17886-17892 (2004).

6 Henkelman, G., Uberuaga, B.P. & Jónsson, H. A climbing image nudged elastic band method for finding saddle points and minimum energy paths. *J. Chem. Phys.* **113**, 9901 (2000).

7 Henkelman, G. & Jónsson, H. A dimer method for finding saddle points on high dimensional potential surfaces using only first derivatives. *J. Chem. Phys.* **111**, 7010 (1999).

8 Zhou, Z. *et al.* The vacuum ultraviolet beamline/endstations at NSRL dedicated to combustion research. *J Synchrotron Radiat* **23**, 1035-1045 (2016).

9 Zhu, Y. *et al.* Online study on the catalytic pyrolysis of bituminous coal over HUSY and HZSM-5 with photoionization time-of-flight mass spectrometry. *Energy Fuels* 2016, **30**, 1598-1604 (2016).

10 Pan, Y. *et al.* Online characterization of isomeric/isobaric components in the gas phase of mainstream cigarette smoke by tunable synchrotron radiation vacuum ultraviolet photoionization time-of-flight mass spectrometry and photoionization efficiency curve simulation. *Anal. Chem.* **85**, 11993-12001 (2013).

11 Qi, F. Combustion chemistry probed by synchrotron VUV photoionization mass spectrometry. *Proc. Combust. Inst.* **34**, 33-63 (2013).

12 Cool, T. A. et al. Photoionization cross sections for reaction intermediates in hydrocarbon combustion. *Int. J. Mass. Spectrom* **247**, 18-27 (2005).

13 Cool, T. A. et al. Studies of a fuel-rich propane flame with photoionization mass spectrometry. *Proc. Combust. Inst.* **30**, 1681-1688 (2005).

14 Hsu, H. C. & Ni, C. K. Vacuum ultraviolet single-photon postionization of amino acids. *Appl. Sci.* **8**, 699 (2008).

15 Haddad, G, N. & Samson, J. Total absorption and photoionization cross sections of water vapor between 100 and 1000 A. *J. Chem. Phys.* **84**,

6623-6626 (1986).

16 Barbaray, J., Contour, J. P. & Mouvier, G. Effects of Nitrogen Dioxide and Water Vapor on Oxidation of Sulfur Dioxide over V205 Particles. 12, 1294-1297 (1978).

17 Warshawsky, A. *et al.* Ion exchange resins for gold cyanide extraction containing a piperazine functionality, 1 Synthesis and physico-chemical properties. *Macromol. Mater. Eng.* **283**, 103-114. (2000)

18 Haber, J. *et al.* ESCA studies of copper oxides and copper molybdates. *J. Solid. State. Chem.* **25**, 207-218 (1978).

19 Venezia, A. M., Bertoncello, R. & Deganello, G. X-Ray photoelectron spectroscopy investigation of pumice-supported nickel catalysts. *Surf. Interface. Anal.* **23**, 239-247 (1995).

20 Wattanakit, C. *et al*. Pulsed electroconversion for highly selective enantiomer synthesis. *Nat. Commun.* **8**, 2087 (2017).

21 Luo, P. *et al*. Constant potential amperometric detection of underivatized amino acids and peptides at a copper electrode. *Anal. Chem.* **63**, 1702-1707 (1991).